PNAS RESEARCH ARTICLE | CELL BIOLOGY ENGINEERING

Implantable 3D printed hydrogels with intrinsic channels for liver tissue engineering

Tyler J. Lieberthal[a], Tatevik Sahakyants[a], Naomi R. Szabo-Wexler[a], Matthew J. Hancock[b], Andrew P. Spann[b], Mark S. Oliver[b], Scott C. Grindy[b], Craig M. Neville[a], and Joseph P. Vacanti[c,d,1]

Affiliations are included on p. 11.

Edited by Joseph DeSimone, Stanford University, Stanford, CA; received March 26, 2024; accepted September 28, 2024

This study presents the design, fabrication, and evaluation of a general platform for the creation of three-dimensional printed devices (3DPDs) for tissue engineering applications. As a demonstration, we modeled the liver with 3DPDs consisting of a pair of parallel millifluidic channels that function as portal-venous (PV) and hepatobiliary (HB) structures. Perfusion of medium or whole blood through the PV channel supports the hepatocyte-containing HB channel. Device computer-aided design was optimized for structural stability, after which 3DPDs were 3D printed in a polyethylene(glycol) diacrylate photoink by digital light processing and evaluated in vitro. The HB channels were subsequently seeded with hepatic cells suspended in a collagen hydrogel. Perfusion of 3DPDs in bioreactors enhanced the viability and function of rat hepatoma cells and were maintained over time, along with improved liver-specific functions. Similar results were observed with primary rat hepatocytes, including significant upregulation of cytochrome p450 activity. Additionally, coculture experiments involving primary rat hepatocytes, endothelial cells, and mesenchymal stem cells in 3DPDs showed enhanced viability, broad liver-specific gene expression, and histological features indicative of liver tissue architecture. In vivo implantation of 3DPDs in a rat renal shunt model demonstrated successful blood flow through the devices without clot formation and maintenance of cell viability. 3D printed designs can be scaled in 3D space, allowing for larger devices with increased cell mass. Overall, these findings highlight the potential of 3DPDs for clinical translation in hepatic support applications.

3D printing | tissue engineering | liver | anastomosis | hydrogel

Significance

Blood perfusion is a significant requirement for tissue viability that greatly limits scalability of potential functional tissue-engineered organ implants. We designed a 3D printed hydrogel device containing parallel millifluidic channels where blood flow supports functional liver tissue through nanoporous material. In vitro, medium actively pumped through the device enhanced viability and function of hepatocytes. After subsequent rounds of design optimization, evaluation of the device in a renal rodent shunt model demonstrated that blood perfusion through the channel significantly enhanced cell viability and function relative to nonperfused implants. The intrinsic architecture of the device facilitates scaling of tissue mass, thus holding promise for therapeutic tissue replacement applications.

Orthotopic liver transplantation stands as the primary effective intervention for patients suffering from acute or chronic liver failure. Despite its success, a severe shortage of donor organs persists, leading to many patients succumbing to their conditions while awaiting transplantation. While the number of liver transplants taking place annually in the United States has gradually increased to 9,234 in 2019, 25,000 patients remain on the waiting list, and over 2,000 die annually without receiving a transplant (1). To bridge this critical gap, bioartificial liver devices have emerged as temporary hepatic assist machines, potentially offering a lifeline to patients awaiting transplantation or native organ repair and regeneration. These devices operate by perfusing the patient's plasma through cartridges containing a human hepatoma cell line or harvested porcine or human hepatocytes embedded in a scaffold. However, despite numerous Phase I/II/III trials, the results have generally fallen short of expectations (2). Limited improvements in clinical benchmarks, such as transient decreases in intracranial pressure and ammonia levels, alongside increases in serum albumin, have failed to demonstrate a statistically significant advantage over simple dialysis (3). This underscores the pressing need for a paradigm shift in the development of technologies addressing advanced liver disease.

Microfabrication techniques and microfluidics have opened a suite of tools available for tissue engineering applications. 3D printing in particular offers the possibility of building de novo tissue architecture with a variety of biologically derived or synthetic polymers. Various 3D printing technologies, including digital light processing (DLP), volumetric printing, and embedded printing, have been employed to generate large scaffolds (4–6). Regardless of the printing or manufacturing modality, integration of large tissue-engineered scaffolds remains a challenge. The limitation of diffusion to adequately perfuse tissues necessitates embedding vascular channel networks, either by engineering millifluidic and microfluidic channels into the design or neovascular ingrowth to generate the channels.

The primary objective in designing an implantable liver device was to create a bioreactor environment that mimics hepatic physiology to offer enhanced support for cell viability and function. Combining 3D printing microfabrication, cell biology, and surgical

Author contributions: T.J.L., T.S., M.J.H., A.P.S., C.M.N., and J.P.V. designed research; T.J.L., T.S., N.R.S.-W., M.J.H., A.P.S., M.S.O., and S.C.G. performed research; T.J.L. and T.S. contributed new reagents/analytic tools; T.J.L., N.R.S.-W., M.J.H., M.S.O., S.C.G., C.M.N., and J.P.V. analyzed data; and T.J.L., T.S., M.J.H., C.M.N., and J.P.V. wrote the paper.

Competing interest statement: J.P.V. equity in 3D BioLabs, LLC. T.J.L., T.S., M.J.H., A.P.S., M.S.O., S.C.G., C.M.N., and J.P.V. hold patents and patent applications related to content in this work.

This article is a PNAS Direct Submission.

[1]To whom correspondence may be addressed. Email: jvacanti@mgb.org.

This article contains supporting information online at https://www.pnas.org/lookup/suppl/doi:10.1073/pnas.2403322121/-/DCSupplemental.

Published November 12, 2024.

techniques into our design strategy, our group has developed a fundamental methodology for a highly scalable bichannel liver assist device intended for direct implantation, with circulatory anastomosis in vivo. Blood flow through a millifluidic network generates mass transport across a nanoporous hydrogel barrier to nourish parenchymal tissue in parallel channels. Device designs were tested in vitro to optimize design choices prior to validation in a renal shunt model.

Results

3D Printed Device (3DPD) Development. The fundamental functional structure of our 3DPD design is a pair of parallel channels: One channel allows for active flow of blood or medium, and the other contains cells. These two compartments simulate a blood vessel and a surrounding parenchymal space. To achieve a physical barrier with chemical permeability, we selected polyethylene(glycol) diacrylate (PEGDA) as the scaffold material due to its printability, polymer availability and uniformity, low immunogenicity, relative mechanical strength, and flexibility for chemical modification. A PEGDA molecular weight of 700 Da was selected to produce a relatively high cross-link density to ensure mechanical strength while maintaining high (80%) porosity (*SI Appendix*, Fig S1*A*).

The basic structural motif of the 3DPD is thus two millifluidic channels separated by a permeable PEGDA barrier, which allows fluid and solute movement between channels. We selected liver as an application; as such, one millifluidic channel recapitulates portal-venous (PV) blood flow, the other hepatobiliary (HB) (Fig. 1*A*).

3DPDs were 3D printed using a LUMEN-X DLP printer, which is a modality ideally suited for fidelity printing of 3D millifluidic and microfluidic channels. A PEGDA scaffold has minimal ability to interact directly with cells due to lack of bioactive chemical structures. Therefore, cells were suspended in a collagen matrix prior to loading into the HB channel and allowed to gel, resulting in a dense suspension of cells in a 3D collagen matrix within the PEGDA hydrogel (Fig. 1*B*).

Channels were printed with 1 mm square cross sections separated by a 300 μm PEGDA porous barrier; the nominal volume of the HB channel was about 20 μL. The intersecting region of the PV and HB channels was about 12 mm long with a total device width of about 25 mm (Fig. 1*C* and *SI Appendix*, Fig. S2 *A–C*).

To connect the 3DPD to external systems (in vitro bioreactors and in vivo vessels), ports for connecting silicone tubing were added to the channel termini. We performed mechanical testing of 3D printed PEGDA dogbone geometries to determine strength in compression and tension. As expected, tension applied normal to 3D printed layers led to failure earlier than tension applied parallel to layers (*SI Appendix*, Fig. S3 *A–D*). The measured material properties were used in a finite element model of the hydrogel port–tube interface which simulated the strain and hoop stress in the hydrogel resulting from the tube overfit—i.e., the tube outer diameters were slightly larger than the port diameter to achieve a snug fit (*SI Appendix*, Fig. S3 *A–H*). By keeping the overfit-induced strain below the strain limit and adding additional wall thickness, we generated optimized port dimensions to allow tubing to fit snugly into the ports while keeping the maximum principal strain in the hydrogel as low as

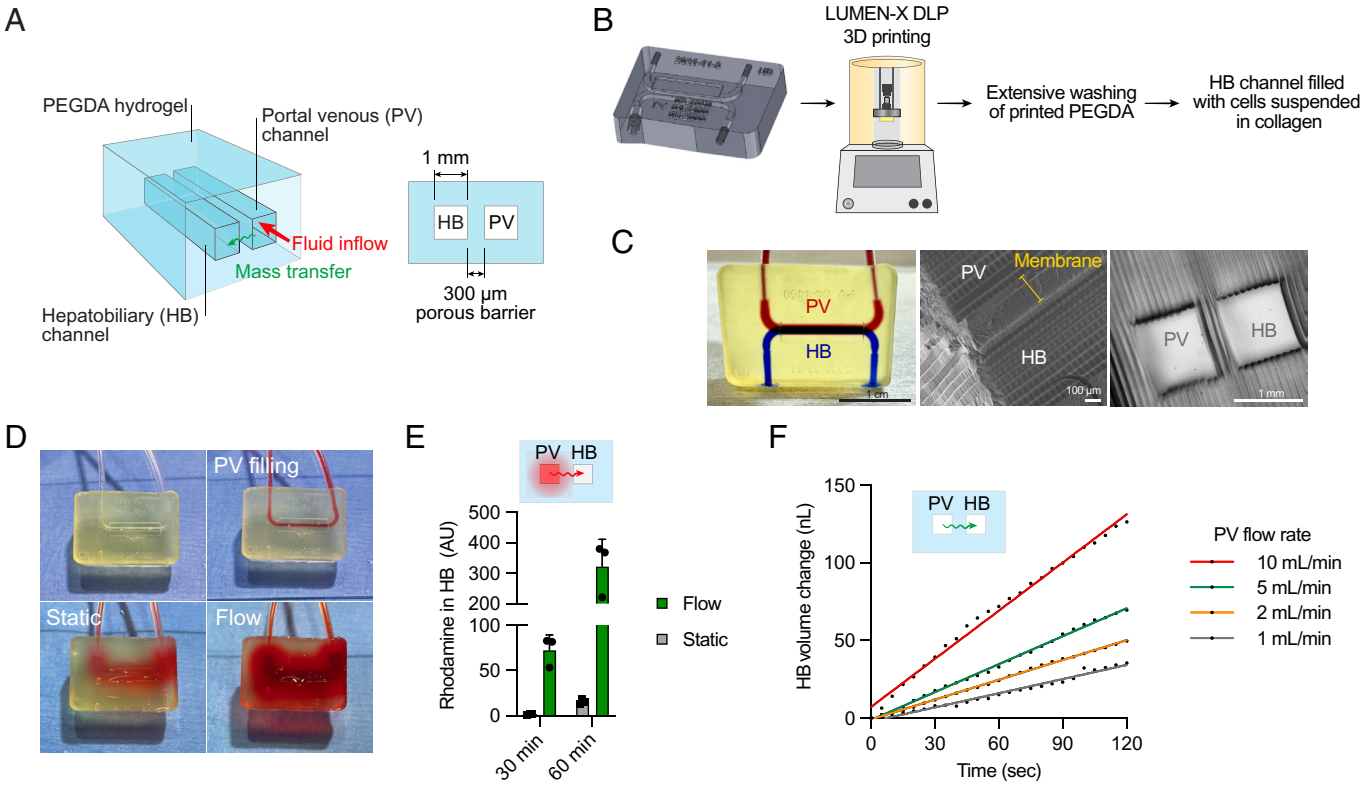

Fig. 1. Design, fabrication, and evaluation of 3DPDs. (*A*) The general design motif of the 3D printed channels consisted of two parallel channels comprising a HB channel and PV channel. Perfusion of the PV channel by blood or medium induces water and small molecule transfer through the nanoporous hydrogel barrier to drain into the HB. (*B*) The workflow to produce 3DPDs included 3D printing from a computer-aided design (CAD) file with a PEGDA photoink on a LUMEN-X DLP printer. Printed devices were then seeded with cells through HB channels in a suspension of collagen hydrogel. (*C*) Finished 3DPDs showing PV channel (red) and HB channel (blue). Scanning electron microscopy (SEM) and brightfield images show channels separated by three printed layers. (*D*) Red dye perfused through the PV channel led to enhanced mass transfer into the bulk of the hydrogel in comparison to nonperfused devices. (*E*) Rhodamine perfusion through the PV was detected in the HB at 30 min and 60 min. Concentrations in the HB were significantly elevated with perfusion. (*F*) Increasing flow rates in the PV led to nL/s flow rates in the HB when the HB outlet was open. Data represent means ± SD for $N = 3$ to 6 devices.

possible to prevent cracking. Due to the low molecular weight of PEGDA, volumetric swelling was limited (*SI Appendix*, Fig. S1*B*), and postprint port dimensions were similar to postswelling dimensions, advantageous for optimizing parameters.

With an optimized port/tube design, the connections were stable well in excess of human systolic pressure (~300 mmHg) without application of adhesives (*SI Appendix*, Fig. S3 *I–K*). Additionally, the HB-PV channel barrier maintained integrity during stringent tube/hydrogel burst pressure testing (*SI Appendix*, Fig. S3*L*). This design was sufficient to provide stable connections for in vitro systems and subsequent in vivo implantation.

Flow enhances chemical transport within the PEGDA hydrogel; as a demonstration, diffusion of red dye into the hydrogel was enhanced when perfused through the PV channel relative to static conditions (Fig. 1*D*). When the PV channel was filled with a solution containing the dye rhodamine, it was readily detected in the HB channel (Fig. 1*E*). Because perfusion of the PV channel maintains a constant high concentration of rhodamine, the difference in total diffusion between static and flow conditions increased with increased time. We also found that a measurable pressure-driven flow could be produced between the PV and HB (Fig. 1*F*). This 3DPD design and material allowed for the mechanical robustness needed for surgical handling while allowing for perfusion between millifluidic channels to support cultured cells.

Perfusion Enhances Viability and Function of Rat Hepatocytes. A custom bioreactor system composed of gas-permeable silastic tubing, modified polypropylene tubes, and a peristaltic pump was developed to evaluate in vitro the ability of 3DPDs to maintain cell viability and essential functions (*SI Appendix*, Fig. S4). 3DPDs were loaded with a high density (20 million cells/mL) of rat hepatoma cells suspended in a collagen gel. Titrated cell densities in 3D collagen gels were cultured in static conditions in glass-bottom dishes to determine the concentration limit beyond which viability is affected. A density higher than this threshold was purposely chosen to provide a challenging environment by which to evaluate potential benefit of perfusion (*SI Appendix*, Fig. S5 *A–D*). Due to the printed size, 3DPDs required multiple days of washing to remove unpolymerized prepolymer components; once completed, the PEGDA was found to be biocompatible (*SI Appendix*, Fig. S5 *E–G*).

Under flow/perfusion conditions, medium was pumped through the PV channel at 1 mL/min, whereas 3DPDs in static conditions were maintained submerged in medium. At the indicated times, cell/collagen matrices were removed from the HB channels for processing. Under static conditions, early time points revealed areas of cell death as indicated by propidium iodide (PI), brightfield, and histological staining (Fig. 2*A*). Whole cell/collagen matrices were also lysed, and adenosine triphosphate (ATP) was quantified as a measure of viability. At 24 h after loading, the high initial cell density led to cell death in static conditions before recovery at 3 and 7 d (Fig. 2*B*). In contrast, perfused devices maintained cell viability and increased in cell density over 1 wk (Fig. 2*C*). Further analysis of early time points showed a relative increase in expression of the proliferation marker gene proliferating cell nuclear antigen (PCNA) for flow conditions. Although the mRNA expression ratios of proapoptosis to antiapoptosis genes Bax/Bcl2 were unchanged, caspase-3/7 enzyme activity was 70% higher without flow (Fig. 2 *D* and *E*).

An important liver function is synthesis and secretion of proteins and compounds by the hepatocyte. Hepatocyte-specific synthetic products secreted into the surrounding hydrogel and medium were measured. Albumin levels, a sensitive marker of secreted proteins, were not affected by perfusion status, but urea production increased in the presence of flow (Fig. 2*F*). Next, gene expression in hepatoma cells cultured in 3DPDs was compared to that in standard tissue culture plastic where diffusion in medium is not limiting. RNA was extracted from cells grown for 7 d in 3DPDs and flasks and analyzed by RT-PCR. Cells cultured in 3DPDs had equivalent or substantially greater gene expression across core hepatocyte functional domains including hepatocyte-specific transcription factors, synthetic products, cytochrome p450s, and metabolic genes (Fig. 2*G*). In a comparison of gene expression from cells in 3DPDs with or without flow, we found p450 genes *CYP1A1* and *CYP3A4* as well as glucose metabolism gene *G6PC* to be differentially induced (Fig. 2*H*). Thus, we confirmed that perfusion in 3DPDs enhanced viability of rat hepatoma cells within devices and promoted gene expression in key hepatocyte-specific categories. Further, cells within 3DPDs exhibited greater gene expression in comparison to standard tissue culture conditions. This is likely due to the superior culture environment within a 3D collagen matrix in terms of substrate composition and stiffness in addition to 3D vs. 2D cell attachment.

Primary Rat Hepatocytes Maintain Viability and Function in 3DPDs. In contrast to cell lines and some other primary cell types, primary hepatocytes are notoriously sensitive in vitro, poorly proliferative, and difficult to maintain for long periods of time. We thus analyzed the behavior of primary rat hepatocytes cultured in 3DPDs. At low hepatocyte densities, total viability as measured by ATP was comparable at day 3 and day 7. At higher cell densities, introduction of flow better maintained cell viability (Fig. 3*A*), and albumin production scaled similarly to viability at these time points (Fig. 3*B*). We also observed these results in cryopreserved primary rat hepatocytes (Fig. 3*C*). Similar to rat hepatoma cells, the expression of select p450 genes and *G6PC* were twofold to sixfold higher with flow in primary hepatocytes (Fig. 3*D*). We confirmed that flow-induced p450 gene expression led to an increase in enzyme activity using a CYP3A4 (human ortholog to rat CYP3A1) activity assay (Fig. 3*E*) and that perfusion of rifampicin through the PV channel could further induce CYP3A4 (Fig. 3*F*).

In this in vitro system with primary rat hepatocytes, we also sought to determine whether perfusion of medium through the PV was sufficient to maintain cell viability. Specifically, in both static and flow setups, 3DPDs are submerged in medium available to cells via bulk diffusion through the hydrogel from the outside, potentially providing a source of glucose and soluble nutrients. However, if 3DPDs are implanted and anastomosed directly to the vasculature, the only significant source of soluble nutrients is the blood in the PV channel; the abdominal cavity likely provides little for bulk diffusion. We therefore designed a perfusion setup in which medium perfuses through the PV but is not available in the environment surrounding the 3DPD and therefore cannot diffuse into the hydrogel via the 3DPD's external boundaries. This setup was compared to the default perfusion setup in which medium is available from both the outside and via the PV channel (Fig. 3*G*). This was also compared to a static setup in which only medium contained in the bulk hydrogel is available to cells. We found that cell viability was equivalent regardless of bulk hydrogel diffusion, provided there was flow in the PV channel. However, in the absence of PV flow, bulk diffusion from medium outside the 3DPD was required to maintain some level of viability (Fig. 3 *H* and *I*). Therefore, we found PV channel perfusion to be necessary and sufficient to maintain cell viability in the 3DPDs.

Cocultures of Hepatocytes, Endothelial Cells (ECs), and Mesenchymal Stem Cells Demonstrate Features of Tissue Architecture and Function. Prior work has demonstrated that primary hepatocytes benefit from coculture with nonparenchymal cell types: In vitro cocultures are longer lasting,

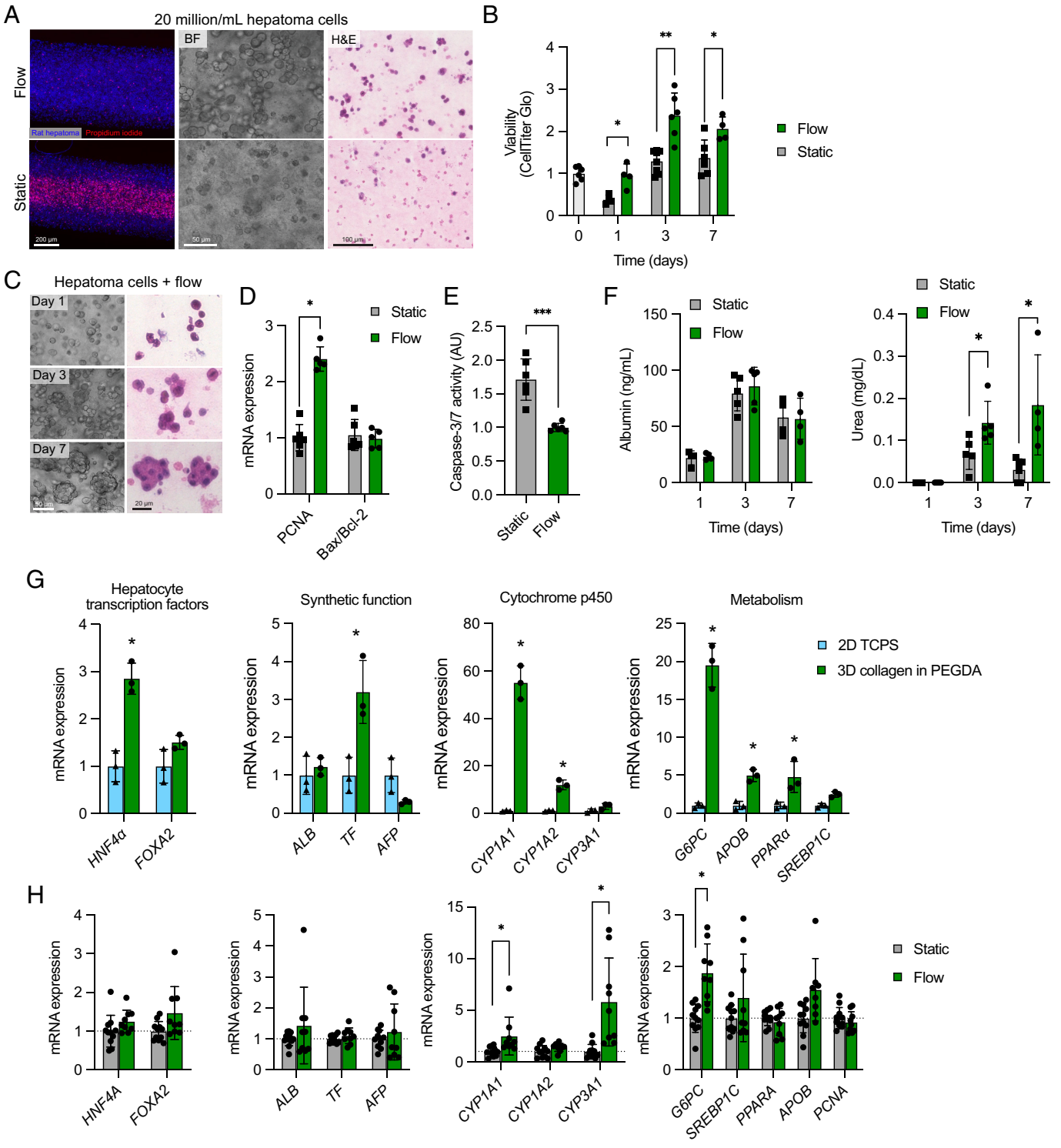

Fig. 2. Perfusion in 3DPDs enhances viability and function of H4-II-E-C3 rat hepatoma cells. (*A*) Fluorescence, brightfield, and hematoxylin and eosin (H&E) staining of cell/collagen hydrogels within 3DPDs. After culture in bioreactors, cell/collagen constructs were removed and stained with PI. Centers of cell death within the center of the collagen hydrogel were observed without perfusion. (*B*) High densities of cells (20 million/mL) were loaded into 3DPDs. ATP was quantified in total 3DPD lysates as a measure of cell viability using CellTiter Glo 3D. Data are plotted as fold changes of arbitrary luminescence units. Perfusion maintained viable cells at 24 h and permitted cell proliferation at 3 and 7 d. (*C*) Brightfield and H&E imaging of rat hepatoma cells at 1, 3, and 7 d in 3DPDs with perfusion. (*D*) Relative gene expression of proliferation (PCNA) and apoptosis (ratio of Bax/Bcl2) between flow and static conditions at 24 h. (*E*) Caspase-3/7 enzyme activity was determined in total 3DPD lysates as a measure of apoptosis. (*F*) Quantification of urea and albumin concentration in medium supernatant and within hydrogel. (*G*) Comparison of gene expression by qPCR of cells cultured in perfused 3DPDs or on tissue culture polystyrene (TCPS). (*H*) qPCR gene expression between perfused and static 3DPDs. Data represent means ± SD for $N = 3$ to 11 devices.

more functional, and develop more tissue-like architecture (7). ECs are a necessary component for development of larger structures and anastomosis of tissue-engineered scaffolds to native tissue. We and others have found that mesenchymal stem cells (MSCs) can stabilize microvascular networks in vitro and in vivo, possibly via differentiation into pericytes (8–10). In evaluating cocultures of primary rat hepatocytes, ECs, and bone-marrow MSCs in 3D matrices, we found that collagen

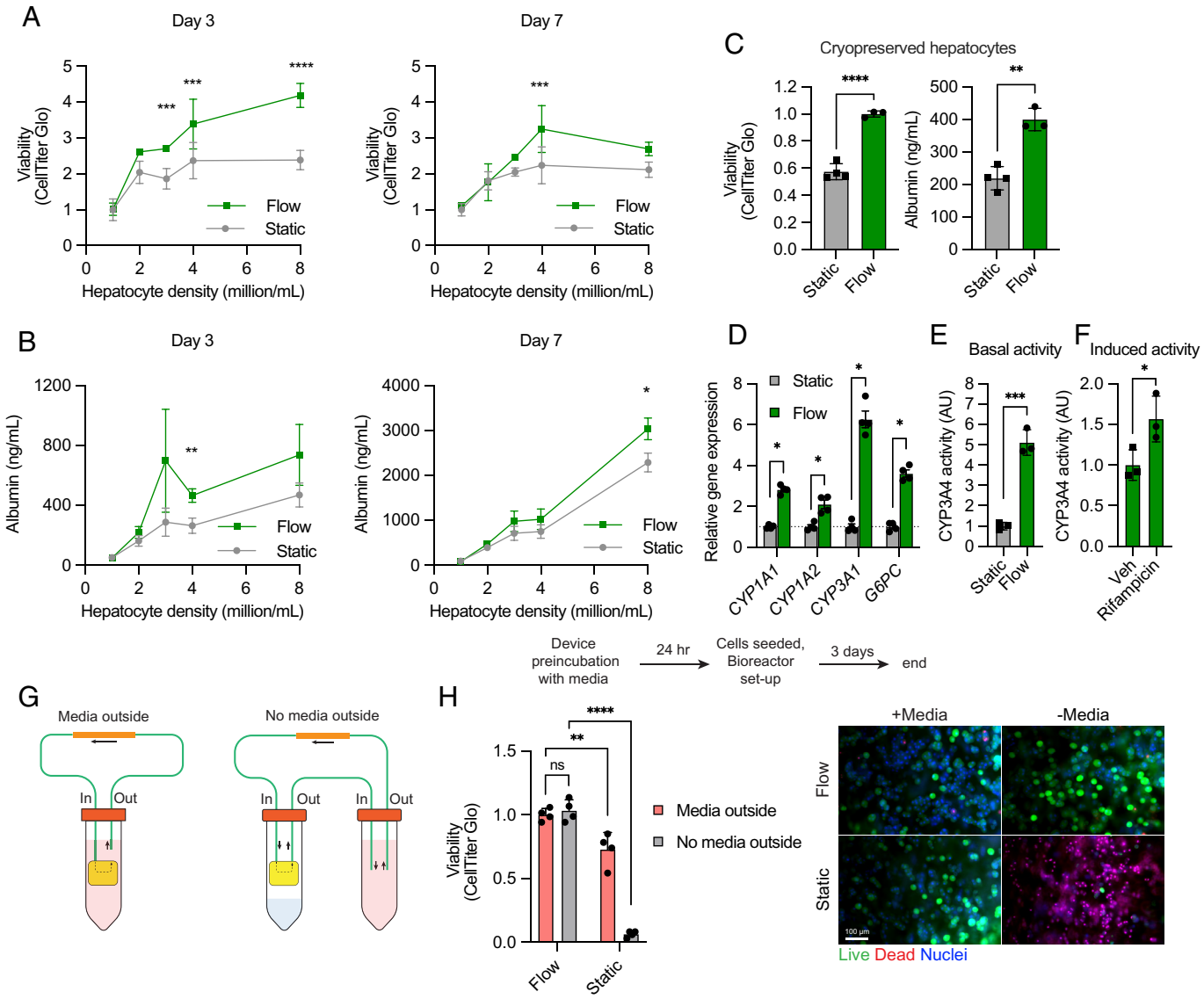

Fig. 3. Perfusion in 3DPDs enhances viability and function of primary rat hepatocytes. (*A* and *B*) Isolated rat hepatocytes suspended in collagen hydrogels at concentrations between 1 and 8 million/mL and loaded into 3DPDs. At 3 and 7 d, viability and albumin production were determined. Viability data are plotted as fold changes of arbitrary luminescence units. (*C*) Viability and albumin production of 4 million/mL cryopreserved hepatocytes determined. (*D*) Relative gene expression of p450 genes (*CYP1A1*, *CYP1A2*, and *CYP3A1*) and *G6PC* in perfused or static 3DPDs. (*E*) 3DPDs were cultured for 3 d, after which cell/collagen gels were removed from HB channels and treated with a CYP3A4 substrate. Enzyme activity was determined with p450-Glo assay. (*F*) Perfused 3DPDs were treated with vehicle or rifampicin for 24 h. CYP3A4 activity was then determined using the p450-Glo assay. (*G*) Experimental setup to determine relative contribution of bulk diffusion through the 3DPD hydrogel. In the default flow setup (*Left*), a peristaltic pump fed medium into the PV channel, after which it drained into the bioreactor chamber. The pump then recirculated medium from the chamber back into the PV. In an alternative setup (*Right*), external medium was in a separate chamber and only entered the 3DPD via the PV channel. Analogous static setups were constructed by submerging devices in medium (static, media outside) or not (static, no media outside). (*H*) Viability of cells in the HB was determined after 3 d of culture in each setup by CellTiter Glo 3D and representative fluorescent microscopy images of cell/collagen hydrogels in 3DPDs treated with calcein AM (green), PI (red), and Hoechst (blue). Data represent means ± SD for $N = 3$ to 8 devices.

alone supported the greatest albumin production in comparison to other naturally derived biomaterials (*SI Appendix*, Fig. S6*A*). In contrast to monocultures of hepatocytes, the cocultures—and MSCs in particular—assist with remodeling and contraction of the gel to produce a more compact 3D culture (*SI Appendix*, Fig. S6*B*) as has been observed previously in cocultures of induced pluripotent stem cells (iPSCs), human umbilical vein endothelial cells (HUVECs), and MSCs (11).

In 3DPDs, we found that flow enhanced the total cell viability and albumin production at day 7 (Fig. 4*A*). The increase in cell number between day 3 and day 7 under flow is likely due to expansion of ECs and MSCs, although some proliferating hepatocytes ($HNF4\alpha^+/Ki67^+$) were noted at day 7 (*SI Appendix*, Fig. S6*C*). Microscopy of the cocultures in 3DPDs with perfusion revealed signs of liver tissue architecture such as hepatocyte rosettes (typical regenerative structures) and apical–basal polarization with localized MRP2 bile transporter expression (Fig. 4*B*).

We then analyzed the effect of flow on gene expression of cocultures in 3DPDs by subjecting day 7 3DPDs to bulk RNA-seq analysis. With flow, gene set enrichment analysis (GSEA) found broad enrichment of liver function-specific gene sets such as xenobiotic metabolism, coagulation, and bile acid metabolism. In contrast, without flow, cells within 3DPDs were enriched in up-regulated genes related to cell cycle, inflammation, IL6/JAK/STAT, and interferon signaling (Fig. 4*C*). Individually selected genes relevant to these liver-specific categories show >twofold increases in hepatocyte synthetic products such as albumin, clotting factors, and bile production. Expression of many p450s were

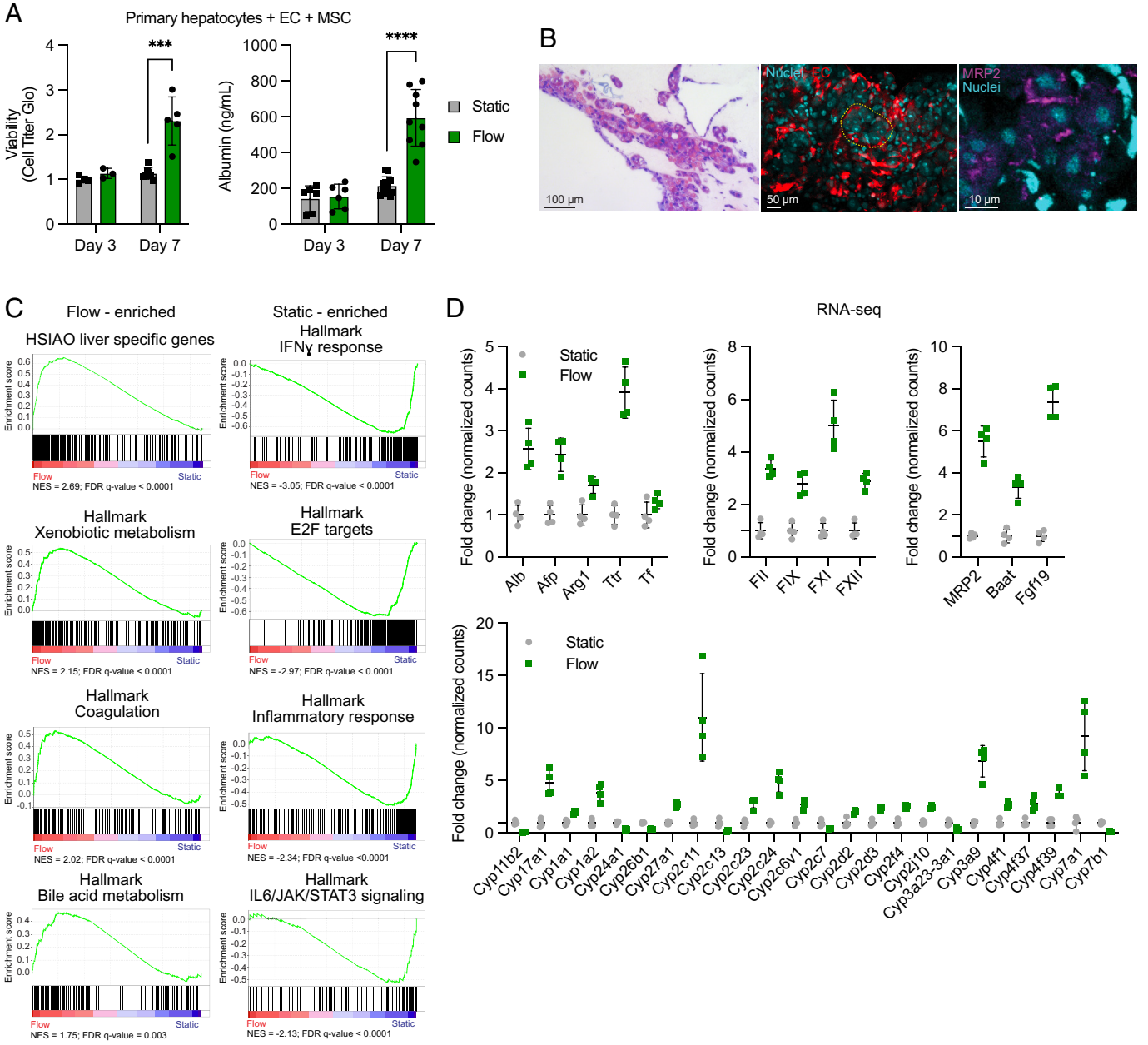

Fig. 4. Perfusion of 3DPDs containing cocultures of primary rat hepatocytes, ECs, and MSCs enhances viability and broad liver-specific gene expression. (*A*) Viability and albumin production of mixed cultures at day 3 and 7. Viability data are plotted as fold changes of arbitrary luminescence units. (*B*) Representative histology of cocultures in 3DPDs with flow. (*Left*) H&E staining, (*Middle*) fluorescence imaging of ECs in red and nuclei in cyan. The circled area indicates hepatocyte rosette structure, (*Right*) fluorescence imaging of MRP2 bile transporter in purple and nuclei in cyan. (*C*) RNA-seq was performed on 3DPDs cultured for 7 d. Normalized expression differences were evaluated against the hallmark and C2 collections of the Human Molecular Signatures Database. (*D*) Select genes from RNA-seq dataset representing liver synthetic products, blood clotting factors, bile synthesis and transport, and p450s. Data represent means ± SD for $N = 3$ to 9 devices.

differentially regulated; most were up-regulated under flow (Fig. 4*D*).

Devices Can Be Anastomosed in Vivo and Maintain Cell Viability. Recently, we reported a surgical method for implanting 3DPDs in a rat liver orthotopic model (12). Using microsurgical techniques, we modified this procedure as a renal shunt in which the 3DPD is connected to the renal artery inflow and renal vein outflow (Fig. 5*A*). The microsurgery involved the cannulation of the left renal artery and vein using separate silastic tubing, each matching the diameter of the respective vessel. The free ends of these tubes were then connected to the inflow and outflow ports of the 3DPD, and blood flow through the 3DPD was established following the left nephrectomy. Critically, this procedure allows the implant to receive direct arterial blood flow through the PV channel, distinguishing it from other implantation methods such as a subcutaneous placement, which often relies on neovascular ingrowth to graft.

Although PEGDA resists protein adsorption and thrombogenesis, rats are known to be hypercoagulable and require additional heparinization. The in vivo 3DPD was thus modified to accommodate an additional port that provides heparin directly to the PV channel. An osmotic heparin pump was therefore implanted into the lumbar subcutaneous pocket and connected via silastic tubing to the additional port. This connection was facilitated through a surgically created tunnel between the lumbar subcutaneous pocket and the abdominal cavity where the 3DPD was positioned. This setup directly and continuously infused heparin into the blood-containing PV channel. Blood flow through the PV channel was rapidly established (<1 s) after the silastic tubes

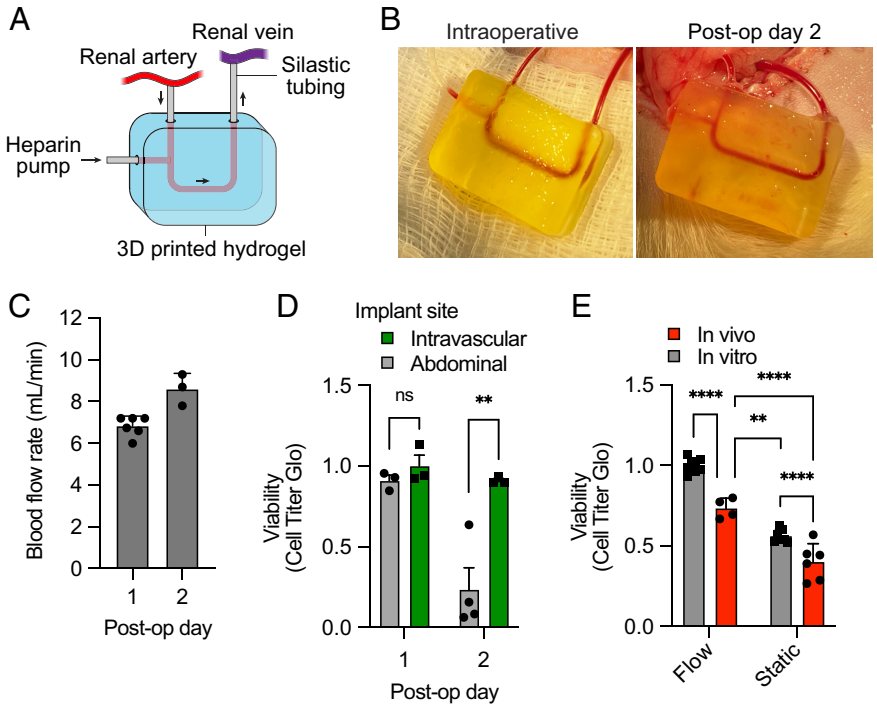

Fig. 5. In vivo implantation of 3DPDs in a rat renal shunt model. (*A*) Schematic of channel design for in vivo implantation. Silastic tubing was used to cannulate the renal artery and vein for inflow and outflow. A separate port was added to allow for continuous heparin delivery into the PV channel via an osmotic pump. (*B*) Representative images of implanted devices after establishing blood flow intraoperatively and when explanting at postoperative day 2. Bright red blood indicates that devices were free of large clots that occluded flow. (*C*) At postoperative days 1 and 2, devices were removed from the abdomen and the outflow tubing was severed. The flow rate through the device was recorded by collecting blood over time. (*D*) Rat hepatoma cells (20 million/mL) were loaded in 3DPDs and, after letting the collagen set, immediately implanted. A second cell-seeded device was placed in the abdomen as a nonperfused control. Devices were recovered at 1 and 2 d to be analyzed by Cell Titer Glo 3D. Viability data are plotted as fold changes of arbitrary luminescence units. (*E*) Rat hepatocytes were isolated and loaded into 3DPDs at 4 million hepatocytes/mL. Devices were cultured in bioreactors for 3 d and then implanted in a littermate intravascularly ("flow") or abdominally ("static") for 1 d prior to analysis. A second group of 3DPDs ("in vitro") were not implanted and continued culture in bioreactors for a fourth day. Data represent means ± SD for $N = 3$ to 6 animals or devices.

were unclamped (Movie S1). Pulsations due to the arterial inflow were observed in the heparin inflow tubing (Movie S2). As both the 3DPD and the pump delivering heparin were internalized, this implementation generated a freely moving animal model suitable for long-term studies.

Effective anticoagulation and continuous blood flow was achieved 2 d postoperatively as indicated by the bright red arterial blood within the PV channel (Fig. 5*B*). The square cross-section of the channel minimizes surface irregularities that may potentially be conducive to initiating thrombosis in comparison to the 3D printed circular cross sections (*SI Appendix*, Fig. S7). The flow rate of blood on postoperative day 1 was 6.83 ± 0.31 mL/min and increased slightly at day 2 (Fig. 5*C*). Our experience has been that flow rate increases over time as the intraoperative vasospasm and the effects of anesthesia resolve. In total, 15 surgeries were successfully performed in which devices were assessed at postoperative day 1. Of those devices, one device later failed due to a dislodged outlet tube leading to intraabdominal bleeding. One device was clotted and no blood flow through the device was observed. Of the six additional devices successfully implanted and assessed at postoperative day 2, two were clotted. We found that optimizing port dimensions was critical in preventing mechanical failures intraoperatively as well as postrecovery of the animal following anesthesia.

3DPDs were loaded with rat hepatoma cells and either implanted in place of the kidney intravascularly or placed in the abdomen without blood flow as analogs of flow and static conditions. We found no difference in cell viability at postoperative day 1 between the intravascular and abdominally placed 3DPDs but a large increase in cell death was apparent at day 2 in abdominally placed 3DPDs (Fig. 5*D*). As rat hepatoma cells are hardier than primary hepatocytes, we speculated that significant numbers of cells could survive at 24 h; indeed, hepatoma cells in static devices without additional media maintained similar viability to static devices with additional media at 24 h in vitro (*SI Appendix*, Fig. S8).

Given primary hepatocytes' sensitivity to culture conditions, we then assessed the viability of primary hepatocytes isolated from Wistar rats, loaded into 3DPDs, and implanted in vivo. Devices were cultured under flow bioreactor conditions for 3 d after which they were implanted in immunocompetent littermates either intravascularly or abdominally. As a control, two groups of devices remained in vitro with or without flow. At postoperative day 1, devices implanted intravascularly contained 1.88-fold more viable hepatocytes compared to abdominally implanted devices. Although in vitro perfused devices contained more viable cells than in vivo intravascular implants, the viability of in vivo perfused devices was significantly greater than both in vitro and in vivo static groups (Fig. 5*E*). Thus, we successfully developed an intravascular implantation of the 3DPDs and demonstrated that blood flow within the implant improved viability compared to nonperfused implants.

Two-Channel Design Can Be Scaled Using Fractal Geometry. To demonstrate that the two-channel design motif can be scaled to accommodate larger cell mass, we employed a fractal geometry to fill 3D space while preserving the proximity of PV channels to HB channels. We hypothesized that cell viability could be maintained in 3DPDs while increasing total cell number due to the perfusability of PV channels.

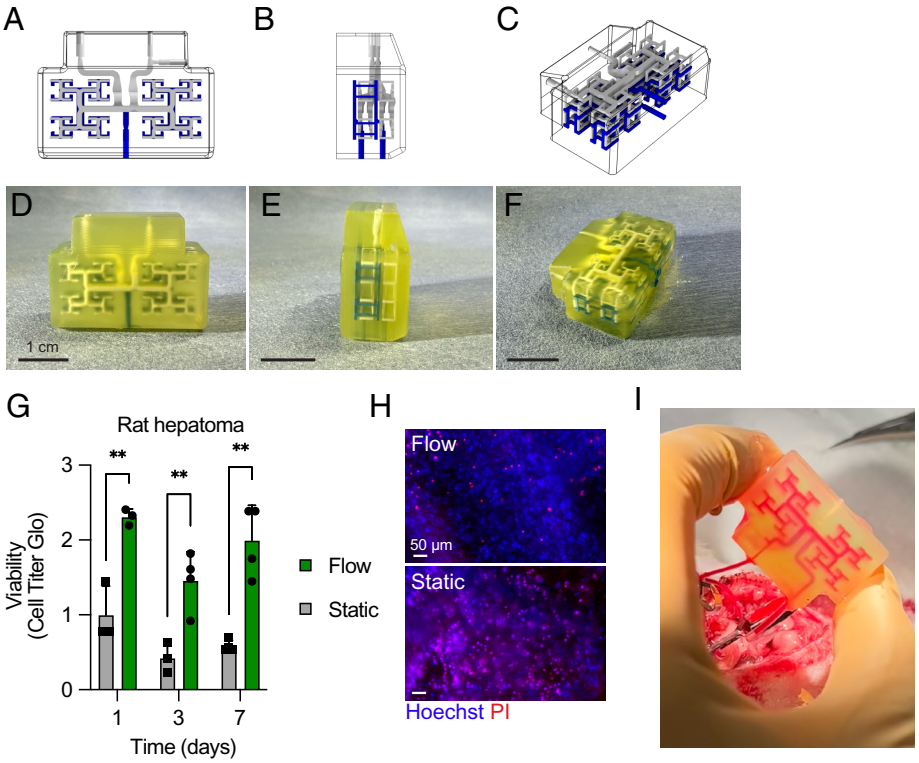

Fig. 6. Scaling of two-channel design with fractal geometry. (*A–C*) CAD images of scaled design with PV channels in gray and HB channels in blue. (*D–F*) 3DPDs with microfluidic and millifluidic channels filled with polyurethane for visualization. PV channels are in white and HB channels in blue. (*G*) Scaled 3DPDs were loaded with rat hepatoma cells, and viability was determined by CellTiter Glo 3D at indicated time points. Data are plotted as fold changes of arbitrary luminescence units. (*H*) Representative PI dead cell staining of cells in HB channels at day 1. (*I*) Intraoperative implantation of scaled 3DPD in a rodent renal shunt model. Data represent means ± SD for $N = 3$ to 4 devices.

The fractal-like channel network geometry consists of one or more generations of T-junctions where a parent channel of diameter D_0 bifurcates at right angles into two child channels with diameters $2^{-1/3}D_0$, the scaling from Murray's law. Higher channel complexity is achieved both by increasing the number of generations within a layer and creating stacks of layers (*SI Appendix*, Fig. S9 *A* and *B*). These layers are fed by a bifurcating distributor channel network and drained by a bifurcating collector channel network, thereby connecting each fractal architecture into a single system. To ensure uniform flow distribution across a layer, the T-junctions at each generation are identical and channel segments connecting T-junctions between two given generations are also identical. To ensure that each layer in the stack is fed the same flow rate, we chose the distributor and collector networks to be identical, as well as the channel segments connecting the distributor/collector networks to layers. Taken together, this design strategy ensures that any flow path through the device has the same length and flow resistance, at least in the low Reynolds number limit.

We designed a scaled 3DPD with four generations in which the smallest channel diameter was 400 µm (Fig. 6 *A–F*). The nominal volume of HB channels containing hepatocytes increased by about 7.7-fold compared to the nonbifurcated original two-channel design with an overall device width of 3 cm. These networks were interfaced with the inlet, outlet, and heparin ports.

A larger bioreactor container was designed to support in vitro perfusion of the PV network with a peristaltic pump (*SI Appendix*, Fig. S9*C*). With 20 million/mL rat hepatoma cells, we verified that perfusion is essential to sustaining this cell density over time (Fig. 6 *G* and *H*). Perfusion of the scaled 3DPD containing primary hepatocytes also significantly increased viability compared to static devices (*SI Appendix*, Fig. S9*D*). We then implanted empty scaled 3DPD devices in the renal shunt rodent model. After unclamping cannula tubing to permit blood flow, all PV channels filled with blood (Fig. 6*I*). Patency to blood flow was maintained at postoperative day 1 with an average flow rate of 4.8 mL/min (N = 2).

Discussion

Here, we describe a general strategy for the application of 3D printed vascular-like structures for direct implantation of cell-laden scaffolds. Small molecules diffuse across a permeable hydrogel barrier separating separate vascular and cell compartments to maintain higher cell counts and increased functionality. Empirical testing of the mass transport properties was conducted in vitro with dye diffusion and with viability of rat hepatocytes in vitro and in vivo. The design of physical connections between tubing and 3DPDs was optimized to provide adequate hydrogel mechanical integrity, bioreactor perfusion, and in vivo implantation.

The inclusion of flow as a cell culture parameter may also benefit hepatocyte function beyond viability alone. In rat hepatoma, primary rat hepatocyte, and coculture loaded 3DPDs, gene expression and p450 activity were highly induced. Induction of p450 activity may be due to higher oxygen tension in the media (13) or the effects of low shear stress, and in hepatocyte culture setups in which medium flow acts directly on monolayers, induction of p450 activity has been observed in numerous studies (14–17). Similarly, perfusion status of hepatic organoids in PEGDA microfluidic arrays modulates phenotype, including p450 and gluconeogenesis (G6PC) (18). Importantly, hepatocytes are highly mechanically sensitive and are not subjected to significant tangential shear flow in tissue; high flow rates in vitro leading to high shear stress can negatively affect hepatocyte function (19). In our 3DPD channel design, 5 mL/min blood flow induces about 20

dyne/cm^2 of wall shear stress (*SI Appendix*, Fig. S10), which is within the normal physiological range of human arteries (20). Importantly, however, the hepatocytes in our system are protected from direct shear stress by the hydrogel barrier, similar to the buffer formed by the space of Disse in vivo.

We chose PEGDA as a suitable proof-of-concept printing material due to properties that were compatible with printability and surgical implantation. As a class of biomaterials, hydrogels often suffer from poor mechanical stability. PEGDA, although more robust than many other hydrogel polymers, can be brittle, making surgical implantation and integration with other materials such as tubing challenging. However, we found that the combination of optimized photoink formulation, printing settings, and mechanical testing supported many successful implantations in rodents that were often very active postoperatively. PEGDA is a popular and easily produced polymer, and a PEGDA photoink can be produced economically which may be critical to the affordability of large 3D printed structures. More generally, other 3D printing techniques may allow printing multiple materials which could better address mechanical stability and permeability (21). Additionally, other photoink polymer blends can exhibit advantageous tough or strain-tolerant mechanical behavior (22, 23).

The choice of PEGDA was also intended to reduce protein and platelet adsorption leading to thrombogenesis. We observed occasional clotting of 3DPDs in vivo, and this was likely related to the accessed vascular site and resulting blood flow rate. Chemical modifications of PEGDA, such as inclusion of arginine-glycine-aspartate (RGD) peptides, or replacement with related polymers such as GelMA, may promote cell–material interactions to endothelialize channel walls for additional protection against thrombogenesis. Biodegradable polymers such as GelMA or ColMA can also be employed to promote neovascular ingrowth into the hydrogel which may further enhance interchannel transport. However, the lack of bioactivity of the PEGDA hydrogel in this work was offset by filling channels with a collagen hydrogel as a cell carrier. Other biomaterial matrices may offer greater benefits to the development of tissue-like architecture; for example, inclusion of fibrin is often used to enhance endothelial tubule formation (24, 25), and optimization of matrix stiffness may be important for coordinating liver tissue development and function (26).

Direct intravascular implantation of 3D printed or microfabricated structures resembling microfluidic devices is not often attempted due to technical difficulties such as thrombogenesis. In previous work, we developed microfluidic arrays and implanted them with direct blood flow from the femoral artery in rats (27). Channels remained patent and perfused for 24 h, but only with regular manual bolus heparin injections. Here, we introduced continuous heparin delivery through osmotic pumps, which were easily integrated into 3DPD millifluidic channels and enabled the 3DPDs to be implanted in the renal artery for up to 2 d. Polydimethylsiloxane microfluidic devices have also been implanted in the femoral artery for up to 3 h (28). GelMA/fibrin gels have been implanted in the carotid artery for 1 wk, albeit with thrombus formation (29). Both Zhang et al. (30) and Szklanny et al. (31) deployed endothelialized degradable polymers in a rodent femoral artery model over 1 and 2 wk. 3D printed PEGDA was also used as an arteriovenous conduit in a large animal model in which different anatomical implantation sites were necessary to prevent clotting (32). Other directly implanted tissue-engineered scaffolds, such as decellularized organs, similarly have susceptibility to clotting without endothelial linings (33, 34).

We observed that intravascular perfusion of 3DPDs was critical for increasing cell viability in comparison to abdominally placed devices not connected to blood flow. Currently, however, even with perfusion, cell death was increased compared to in vitro devices at matched time points. Several factors may contribute to this phenomenon, including reperfusion injury resulting in inflammatory cytokines and the use of allogenic cells in an immunocompetent rodent model. In ongoing work, we are developing protocols for use of autologous primary and stem cells, as well as appropriate surgical management.

We also note that this current design, in which parenchymal cells are contained within a millifluidic channel, constitutes a second fluidic network in addition to the blood-containing PV channel. In an ideal application in a surgical model, HB terminal ports could be connected via tubing to an existing bile network, thus allowing bile produced by loaded cells to drain into the biliary system.

A second goal of current work focuses on iterating and scaling the parallel channel motif to increase channel volumes and therefore the cell mass deliverable in an implant. Whereas reliance on diffusion by nonperfusable or avascular constructs limits scaling, we hypothesize that the inclusion of sufficiently dense millifluidic channels can sustain tissue deep within large implants. Indeed, we observed that fractally scaled 3DPDs demonstrate an increased dependence on flow for cell survival in comparison to the smaller two-channel design. Suitable surgical support systems are currently being developed to evaluate these larger scaled implants in a large animal model.

Materials and Methods

Experimental Setup. The design for a bichannel 3D millifluidic device to support liver cell survival and function was constructed in SolidWorks® and synthesized of poly(ethylene glycol) diacrylate with a direct light 3D printer. One channel (HB) was designed to be seeded with liver cells suspended in a hydrogel. The second channel (PV) supports the cells with medium or blood. Active laminar flow brings fresh soluble factors to and removes soluble waste from the PV side of the PV-HB membrane. The fresh soluble factors then diffuse through the membrane to reach cells in the HB channel, and vice versa for the waste factors. The device is designed with ports to readily allow anastomosis to a peristaltic pump or host vasculature upon implantation.

Multiple parameters potentially influencing hepatocyte survival and function were evaluated during optimization. These variables included cell density, biomatrix composition, inclusion of nonparenchymal cell types, and the flow of medium and blood. Evaluation included both general cell physiology and liver-specific functions.

3D Printing. Computer-aided design files of 3DPDs were constructed in SolidWorks and printed on a LUMEN-X DLP printer using 100 μm layer resolution polymerized at 405 nm. The photoink formulation was 20% PEGDA molecular weight 700 Da, 0.5 wt% lithium phenyl-2,4,6-trimethylbenzoylphosphinate, 2 mM tartrazine, and 10% 10× phosphate buffered saline (PBS). Each layer was ultraviolet (UV) polymerized for 3.5 s for a total print time of ~15 min. After printing, completed parts were sterilized in 70% ethanol for 24 h and washed extensively with large volumes of PBS.

Cell Culture and Isolation. H4-II-E-C3 rat hepatoma cells were obtained from American Type Culture Collection (ATCC) and cultured in high glucose Dulbecco's Modified Eagle Medium (DMEM), 20% horse serum, 5% fetal bovine serum, and 1% penicillin/streptomycin. Rat liver ECs were obtained from Cell Biologics and cultured in endothelial growth medium (EGM-2, Promocell). Rat bone-marrow mesenchymal stem cells (BM-MSCs) were either obtained from Cell Biologics or isolated in-house from rat femurs and tibias according to established protocols (35). BM-MSCs were cultured in StemXVivo and used below passage 7.

Primary rat hepatocytes were isolated according to previous protocols (36). Briefly, 2 to 3 mo old Wistar rats were used in accordance with the Charles River Accelerator and Development Lab Institutional Animal Care and Use Committee (IACUC). Animals were anesthetized with isoflurane and intravascularly injected with a bolus of heparin. The portal vein was cannulated and the liver flushed with

lactated Ringer's solution containing mannitol and heparin. After transport on ice, livers continued perfusion with cation-free Hank's Balanced Salt Solution (HBSS) with ethylene glycol-bis(β-aminoethyl ether)-N,N,N′,N′-tetraacetic acid, followed by cation-containing HBSS, and a 0.05% collagenase IV (Sigma C5138) digestion buffer. Following digestion, livers were minced with scissors and washed with HBSS at 50 × *g*. The hepatocyte fraction was further purified in a 50% Percoll gradient. Isolations generally yielded >90% viability.

Device Loading and Bioreactor Setup. Cells were introduced to the HB millifluidic compartment of the 3DPD by suspending the cells in a solution of rat tail collagen and pipetting the mix into the channel. A 3 mg/mL collagen solution was prepared by mixing high concentration rat tail collagen (Advanced Biomatrix, 10 mg/mL), 5× DMEM, 7.5% sodium bicarbonate, and 100 mM 2-[4-(2-hydroxyethyl) piperazin-1-yl]ethanesulfonic acid (HEPES). For H4-II-E-C3 rat hepatoma experiments, the final cell density in the collagen matrix was 20 million/mL. For primary rat hepatocyte monocultures, a density of 4 million cells/mL was used unless otherwise indicated. For coculture experiments, 1 million hepatocytes/mL were mixed with ECs and mesenchymal stem cells at a 4:2:1 ratio.

Devices were incubated at 37 °C for 1 h to allow the collagen to set. To prevent abdominal blood from entering the cell compartment channels for in vivo implantations, the inlet and outlet ports were plugged with silastic tubing filled with silicone glue.

In vitro bioreactor chambers were constructed using 50 mL conical tubes. Holes were drilled in the cap of a tube to introduce inlet and outlet tubing. A third hole was created to introduce a sterile vent filter capsule. Approximately 250 cm of platinum-cured silicone tubing (ID 1/32″, OD 1/16″) was connected to white/white stop tubing (PharMed BPT) clipped into a Harvard Apparatus P-70 peristaltic pump. The silicone tubing was connected to 3DPDs, and 30 mL of media was pumped through the PV millifluidic channel. Unless otherwise indicated, a flow rate of 1 mL/min was established. For bioreactor setups that contained no external medium, a separate tube containing 30 mL of medium was used to recirculate the medium within the device channels. To maintain a humidified environment, gauze soaked with PBS was placed at the bottom of the conical tube. 3DPDs in flow or static conditions were suspended above soaked gauze to prevent contact between the gauze and 3DPD hydrogel.

For all bioreactor experiments, serum-free hepatocyte growth medium (HGM, Lonza) was used. In coculture experiments, HGM was mixed 1:1 with EGM-2.

Device Characterization. Acellular hydrogel devices were cut with a razor blade to expose internal channels and prepared for scanning electron microscopy by an ethanol dehydration series followed by hexamethyldisilazane and vacuum desiccation. Hydrogel pieces were sputter coated with Au/Pd and imaged on a Zeiss Gemini Sigma 300 VP FE-SEM.

To determine burst pressure of tube-hydrogel connection, a syringe pump (Harvard Apparatus) injected PBS through the inlet tubing at 0.5 mL/min. The outlet tubing was clamped, and the heparin port tubing terminated at a digital pressure sensor. As the syringe pump generated pressure within the device, pressure measurements were recorded.

The ability of small molecules to diffuse through the hydrogel barrier between channels was assessed by perfusing a rhodamine solution through the PV channel with a positive pressure displacement pump (Lee Company). At indicated time points, fluid was collected from the HB channel and rhodamine concentration was determined by reading fluorescence at 526/550 ex/em.

Mechanical characterization of PEGDA hydrogel was conducted using 1.5 cm cubes for compression tests and dogbone geometries for tensile tests. The data were obtained on a TA Instruments Discovery HR 20 Hybrid Rheometer using tension and compression geometries and analyzed with TRIOS software. Tension measurements were performed at a constant linear rate of 20 μm/s; compression measurements were performed at a constant linear rate of 10 μm/s.

Hydrogel swelling parameters were obtained by 3D printing cylinders (1.5 cm diameter, 1 cm height). Gels were weighed or measured for volume before and after swelling in water or PBS. Eluted photomask (tartrazine) was measured by absorbance at 430 nm and quantified with a standard curve.

Surgical Implants. All animal experiments were reviewed and approved by the IACUC. Male Wistar rats (Crl:WI Wistar rats; RRID:RG_737929; Charles River Laboratories, Wilmington, MA) weighing 350 to 450 g were habituated for a minimum of 3 d before use in experiments. Animals were maintained on a 12-h light/12-h dark cycle and given rat chow and water ad libitum. Rats were housed in pairs before surgery and individually after surgery to enable undisturbed recovery.

We previously described in detail a procedure for anastomosing 3D printed hydrogel devices as a liver orthotopic implant in a rat (12). Here, we adapted this surgical technique to supply the device with blood originating from the renal artery and draining into the renal vein. The animals were initially anesthetized using isoflurane, with induction at 4% and maintenance between 1.5 to 2%, supplemented with an oxygen flow of 1 L/min, administered via a nose cone connected to an anesthesia machine. Subsequently, a subcutaneous pocket was created in the lumbar area, adequately sized to accommodate an Alzet 2ML1 pump (Durect #0000323), which was prefilled and primed with a heparin sodium solution (1,000 United States Pharmacopeia (USP) units/mL, Sagent Pharmaceuticals #25021-400-10). A transverse incision, measuring 3 to 4 cm, was then executed in the left lower abdominal quadrant to reveal the left kidney along with its vasculature. This was followed by the creation of a 7 to 8 cm tunnel traversing the left lateral lumbar region, designed specifically to house a silicone tube linking the Alzet pump to the abdominal cavity. Under the magnification provided by a Leica S9i stereomicroscope (Leica Microsystems #10450816), employing microsurgical techniques, the left renal artery and vein were meticulously dissected and isolated through blunt dissection. Cannulation was performed using platinum-cured silicone tubing, with inner diameters of 0.51 mm and 0.76 mm for the renal artery and vein, respectively. The left ureter was securely ligated. The left kidney was subsequently bluntly dissected, externalized, and excised. Within the abdominal cavity, two cell-loaded 3DPDs were placed; one was connected to arterial inflow, venous outflow, and heparin silicone tubes, receiving blood flow through the PV channel, while the other was positioned intraabdominally without blood flow. At postoperative days 1 and 2, blood flow rate was determined by cutting the outlet tubing and collecting the outflow.

Luminescent Assays. Following indicated time points, the cell/collagen construct was manually removed from millifluidic channels. The CellTiter-Glo 3D Cell Viability Assay (Promega) was used to determine cell viability and Caspase-Glo 3/7 Assay System (Promega) for apoptotic activity, with some modifications. For ATP-based viability determination, cell/collagen constructs were lysed in 10% trichloroacetic acid for 20 min on a plate shaker. For caspase-3/7-based apoptosis determination, cell/collagen constructs were lysed in Caspase Cell Lysis Buffer (Enzo Life Sciences). Lysate supernatants were then added to 50% diluted CellTiter Glo or Caspase-Glo reagents. Luminescence was read with a SpectraMax M5 plate reader at 0.5 s integration.

The p450-Glo CYP3A4 activity assay (Promega) was used according to the manufacturer's instructions with modifications. Where indicated, p450 activity was induced with 25 μM rifampicin for 24 h. Cell/collagen constructs were removed from channels and incubated with luciferase substrate for 1 h. One volume of lytic detection reagent was added to wells and incubated for 20 min on a shaker. Lysates were read at 0.5 s integration.

Viability Determination. Nonviable cells were identified by PI staining and fluorescent imaging. In some cases, total cells were determined by staining with CellTracker Deep Red prior to cell loading or with end point calcein AM and Hoechst 33342. Images were acquired on a Zeiss 200 epifluorescent microscope.

Albumin ELISA and Urea Assay. Following indicated time points, conditioned medium from bioreactors was collected. To ensure quantification of total albumin and urea production, the 3D printed hydrogel device was crushed, and any hydrogel-trapped albumin/urea was allowed to elute into the media overnight at 4 °C. Supernatants were centrifuged to remove debris and used in a rat albumin enzyme-linked immunosorbent assay (ELISA) kit (Immunology Consultants Laboratory) or QuantiChrom Urea Assay Kit (Bioassay Systems).

RT-qPCR and RNA-seq. RNA was extracted from cells using Trizol and purified using the RNeasy Plus Universal Mini Kit (Qiagen). cDNA was synthesized using the High-Capacity cDNA Reverse Transcription Kit (Applied Biosystems) with 100 ng input RNA. qPCR was run on a StepOne Plus (Applied Biosystems) using SYBR green reagent. Gene expression differences were calculated using the $2^{-\Delta\Delta Ct}$ method with 18S housekeeping gene. Primer sequences are listed in *SI Appendix*, Table S1.

RNA-seq library preparation with polyA selection, sequencing (Illumina HiSeq 2 × 150bp), and mapping was performed by Azenta Life Sciences. Sequence reads were trimmed to remove possible adapter sequences and nucleotides with poor quality using Trimmomatic v.0.36. The trimmed reads were mapped to the Rattus norvegicus Rnor6.0 reference genome available on ENSEMBL using the STAR aligner v.2.5.2b. Relative gene expression analysis and GSEA were determined using the DEseq2 and GSEA module of GenePattern (37). For GSEA, normalized counts were compared against the hallmark and C2 gene sets in the Human Molecular Signatures Database.

Histology and Staining. Cell/collagen constructs were fixed in 4% paraformaldehyde (PFA) and embedded in either paraffin or optimal cutting temperature (OCT). Paraffin sections were used for hematoxylin and eosin staining. Cryosections were used for immunofluorescence. The following antibodies were used: MRP2 (Santa Cruz sc–59611), hepatocyte nuclear factor 4 alpha (HNF4α) (ThermoFisher MA1–199), and Ki67 (Abcam ab16667).

Statistical Analysis. The data were expressed as mean ± SD and plotted in GraphPad Prism 10. Where present, each data point in a bar/scatter dot plot represents an individual 3DPD. Assays with arbitrary unit readouts (e.g., luminescent assays) were normalized such that flow or static experimental groups had a value of 1 such that experimental groups are expressed as fold changes. Figs. 3*H* and 5*E* were analyzed by a two-way ANOVA with multiple comparisons correction using the Holm–Šídák method. Figs. 2 *B*, *D*, and *F–H*, 3 *A*, *B*, and *D*, 4*A*, 5*D*, and 6*G* were analyzed by multiple unpaired *t* tests with the Holm–Šídák correction. Figs. 2 *E* and 3 *C*, *E*, and *F* were analyzed by unpaired *t* tests. A *P*-value < 0.05 was taken to be statistically significant. The following notations were used: $****P < 0.0001$, $***P < 0.001$, $**P < 0.01$, and $*P < 0.05$.

Data, Materials, and Software Availability. All study data are included in the article and/or supporting information.

ACKNOWLEDGMENTS. We thank Janet LaChance for administrative assistance and Zaya Byambaa for technical support. We thank Nicole Mattson, Eric Schmitt, Riccardo Vietri, and Wen Li for assistance with device preparation. Hydrogel mechanical characterization was performed in part at the Harvard University Center for Nanoscale Systems, a member of the National Nanotechnology Coordinated Infrastructure Network, which is supported by the NSF under NSF award no. ECCS–2025158.

Author affiliations: [a]3D BioLabs, Chadds Ford, PA 19317; [b]Veryst Engineering, Needham, MA 02492; [c]Department of Surgery, Massachusetts General Hospital, Boston, MA 02114; and [d]Department of Surgery, Harvard Medical School, Boston, MA 02115

1. A. J. Kwong *et al.*, OPTN/SRTR 2021 annual data report: Liver. *Am. J. Transplant.* **23**, S178–S263 (2023).
2. Y. T. He, Y. N. Qi, B. Q. Zhang, J. B. Li, J. Bao, Bioartificial liver support systems for acute liver failure: A systematic review and meta-analysis of the clinical and preclinical literature. *World J. Gastroenterol.* **25**, 3634–3648 (2019).
3. A. Kanjo *et al.*, Efficacy and safety of liver support devices in acute and hyperacute liver failure: A systematic review and network meta-analysis. *Sci. Rep.* **11**, 4189 (2021).
4. B. Grigoryan *et al.*, Multivascular networks and functional intravascular topologies within biocompatible hydrogels. *Science* **364**, 458–464 (2019).
5. P. N. Bernal *et al.*, Volumetric bioprinting of complex living-tissue constructs within seconds. *Adv. Mater.* **31**, e1904209 (2019).
6. A. Lee *et al.*, 3D bioprinting of collagen to rebuild components of the human heart. *Science* **365**, 482–487 (2019).
7. S. N. Bhatia, U. J. Balis, M. L. Yarmush, M. Toner, Effect of cell-cell interactions in preservation of cellular phenotype: Cocultivation of hepatocytes and nonparenchymal cells. *FASEB J.* **13**, 1883–1900 (1999).
8. P. Au, J. Tam, D. Fukumura, R. K. Jain, Bone marrow-derived mesenchymal stem cells facilitate engineering of long-lasting functional vasculature. *Blood* **111**, 4551–4558 (2008).
9. O. Tsigkou *et al.*, Engineered vascularized bone grafts. *Proc. Natl. Acad. Sci. U.S.A.* **107**, 3311–3316 (2010).
10. X. Cai *et al.*, Bone marrow derived pluripotent cells are pericytes which contribute to vascularization. *Stem. Cell Rev. Rep.* **5**, 437–445 (2009).
11. T. Takebe *et al.*, Vascularized and functional human liver from an iPSC-derived organ bud transplant. *Nature* **499**, 481–484 (2013).
12. T. Sahakyants *et al.*, Rodent model for orthotopic implantation of engineered liver devices. *Tissue Eng. Part C Methods* **29**, 20–29 (2023).
13. S. Kidambi *et al.*, Oxygen-mediated enhancement of primary hepatocyte metabolism, functional polarization, gene expression, and drug clearance. *Proc. Natl. Acad. Sci. U.S.A.* **106**, 15714–15719 (2009).
14. B. Vinci *et al.*, Modular bioreactor for primary human hepatocyte culture: Medium flow stimulates expression and activity of detoxification genes. *Biotechnol. J.* **6**, 554–564 (2011).
15. I. Shvartsman, T. Dvir, T. Harel-Adar, S. Cohen, Perfusion cell seeding and cultivation induce the assembly of thick and functional hepatocellular tissue-like construct. *Tissue Eng. Part A* **15**, 751–760 (2009).
16. P. Roy, J. Washizu, A. W. Tilles, M. L. Yarmush, M. Toner, Effect of flow on the detoxification function of rat hepatocytes in a bioartificial liver reactor. *Cell Transplant.* **10**, 609–614 (2001).
17. E. Novik, T. J. Maguire, P. Chao, K. C. Cheng, M. L. Yarmush, A microfluidic hepatic coculture platform for cell-based drug metabolism studies. *Biochem. Pharmacol.* **79**, 1036–1044 (2010).
18. S. Grebenyuk *et al.*, Large-scale perfused tissues via synthetic 3D soft microfluidics. *Nat. Commun.* **14**, 193 (2023).
19. A. W. Tilles, H. Baskaran, P. Roy, M. L. Yarmush, M. Toner, Effects of oxygenation and flow on the viability and function of rat hepatocytes cocultured in a microchannel flat-plate bioreactor. *Biotechnol. Bioeng.* **73**, 379–389 (2001).
20. A. M. Malek, S. L. Alper, S. Izumo, Hemodynamic shear stress and its role in atherosclerosis. *JAMA* **282**, 2035–2042 (1999).
21. Y. T. Kim, A. Ahmadianyazdi, A. Folch, A "print-pause-print" protocol for 3D printing microfluidics using multimaterial stereolithography. *Nat. Protoc.* **18**, 1243–1259 (2023).
22. J. Y. Sun *et al.*, Highly stretchable and tough hydrogels. *Nature* **489**, 133–136 (2012).
23. Q. Ge *et al.*, 3D printing of highly stretchable hydrogel with diverse UV curable polymers. *Sci. Adv.* **7**, eaba4261 (2021).
24. D. B. Kolesky, K. A. Homan, M. A. Skylar-Scott, J. A. Lewis, Three-dimensional bioprinting of thick vascularized tissues. *Proc. Natl. Acad. Sci. U.S.A.* **113**, 3179–3184 (2016).
25. T. A. Ahmed, E. V. Dare, M. Hincke, Fibrin: A versatile scaffold for tissue engineering applications. *Tissue Eng. Part B Rev.* **14**, 199–215 (2008).
26. G. Sorrentino *et al.*, Mechano-modulatory synthetic niches for liver organoid derivation. *Nat. Commun.* **11**, 3416 (2020).
27. W. M. Hsu *et al.*, Liver-assist device with a microfluidics-based vascular bed in an animal model. *Ann. Surg.* **252**, 351–357 (2010).
28. R. Sooppan *et al.*, In vivo anastomosis and perfusion of a three-dimensionally-printed construct containing microchannel networks. *Tissue Eng. Part C Methods* **22**, 1–7 (2016).
29. X. Liu *et al.*, 3D liver tissue model with branched vascular networks by multimaterial bioprinting. *Adv. Healthc. Mater.* **10**, e2101405 (2021).
30. B. Zhang *et al.*, Biodegradable scaffold with built-in vasculature for organ-on-a-chip engineering and direct surgical anastomosis. *Nat. Mater.* **15**, 669–678 (2016).
31. A. A. Szklanny *et al.*, 3D bioprinting of engineered tissue flaps with hierarchical vessel networks (vesselnet) for direct host-to-implant perfusion. *Adv. Mater.* **33**, e2102661 (2021).
32. N. T. N. Galvan *et al.*, Blood flow within bioengineered 3D printed vascular constructs using the porcine model. *Front. Cardiovasc. Med.* **8**, 629313 (2021).
33. B. E. Uygun *et al.*, Organ reengineering through development of a transplantable recellularized liver graft using decellularized liver matrix. *Nat. Med.* **16**, 814–820 (2010).
34. J. Devalliere, Y. Chen, K. Dooley, M. L. Yarmush, B. E. Uygun, Improving functional re-endothelialization of acellular liver scaffold using REDV cell-binding domain. *Acta Biomater.* **78**, 151–164 (2018).
35. M. Soleimani, S. Nadri, A protocol for isolation and culture of mesenchymal stem cells from mouse bone marrow. *Nat. Protoc.* **4**, 102–106 (2009).
36. P. O. Seglen, Preparation of isolated rat liver cells. *Methods Cell Biol.* **13**, 29–83 (1976).
37. M. Reich *et al.*, GenePattern 2.0. *Nat. Genet.* **38**, 500–501 (2006).